

Chapter 3

The 10-fold d -Al-Ni-Co Surface

This chapter begins with a short review on investigations of clean surfaces. Then, the results of our experiments on the 10-fold d -Al_{71.8}Ni_{14.8}Co_{13.4} surface by three different techniques, spot profile analyzing low energy electron diffraction (SPA-LEED), He atom scattering (HAS), and Scanning tunneling microscopy (STM) are discussed.

Early work in the field of quasicrystal surfaces mainly focused on surface preparation, determination of surface composition, and characterization of clean surfaces of i -Al-Pd-Mn (see [6, 20] for a review). Recently, there have been several reports on decagonal quasicrystal surfaces, especially on the 10-fold surface of d -Al-Ni-Co. These investigations reveal that the surfaces obtained strongly depend on the specific preparation methods. As in periodic crystals, sputter-annealing and cleaving in UHV have been employed to prepare quasicrystal surfaces. Sputter-annealing can produce high quality surfaces suitable for various surface sensitive techniques including the extremely surface sensitive He atom scattering [19, 33, 122]. The surfaces prepared by this method often show terrace-step structures. Scanning tunneling microscopy of these surfaces reveals a typical corrugation of several tenths of an Angstrom and terrace widths up to several hundred Angstroms [6, and find references therein]. Diffraction techniques like X-ray photoelectron diffraction (XPD), low energy electron diffraction, and He atom scattering show that terraces possess a perfect long range, quasicrystalline order. The terraces closely reflect the structure of underlying bulk [6, also see Sections 3.1, 3.2, and Chapter 4].

There has been a great effort to resolve atomic structures of sputter-annealed surfaces by scanning tunneling microscopy. The first experiments were reported by Kortan *et al.* in 1990.

They investigated the 10-fold surface of *d*-Al-Cu-Co [16, 17] and observed atomically flat, wide terraces separated by steps of bulk expected height. The observed structure within the terraces was explained in terms of tiling models. Schaub *et al.* reported the first STM study of icosahedral quasicrystals. They found that the 5-fold surface of *i*-Al-Pd-Mn exhibits flat terraces with some pentagonal holes and stars. The steps are of two different heights forming a part of a Fibonacci sequence.

Recent reports on the 5-fold surface of *i*-Al-Pd-Mn by Barbier *et al.* [19], on the 5-fold surface of *i*-Al-Cu-Fe by Cai *et al.* [123], the 10-fold surface of *d*-Al-Ni-Co by McGrath *et al.* [20] and the 10-fold and 2-fold surfaces of *d*-Al-Ni-Co by Kishida *et al.* [18] also show very flat surfaces with 5-fold and/or 10-fold motives. However, atomic resolution of the images of these surfaces is not far better than previous results. Barbier *et al.* [19] found three different step heights scaled with each others by τ in contrast to the previous observation of two different heights. Kishida *et al.* [18] have detected a very low density of interlayer phason defects on the 2-fold *d*-Al-Ni-Co surface. In the present investigations of the 10-fold *d*-Al-Ni-Co surface by low temperature STM, a random (Penrose) tiling is identified on a large area of the surface (see Section 3.3).

3.1 Spot Profile Analyzing Low Energy Electron Diffraction

Surface Preparation and Measurement Conditions

A large grain *d*-Al_{71.8}Ni_{14.8}Co_{13.4} sample grown by the Czochralski method [124] was cut perpendicular to the 10-fold axis. After polishing the surface by diamond paste, the sample was attached directly on a resistive heater by using tantalum foil and mounted in the experimental chamber (base pressure 1×10^{-10} mbar after bake out). The surface was prepared by several cycles of sputtering and annealing. The sample was sputtered (Ne⁺, 1.5 kV and 6 μ A) for 30 minutes and subsequently annealed for 15-25 minutes at 600-650 °C. The sample was cooled to 95 K during measurements to reduce inelastic scattering (Debye Waller attenuation).

SPA-LEED images of the clean surface were taken at different electron energies. Sharp electron diffraction patterns at the above described sputter-annealing conditions were obtained in a energy range of 40-80 eV. As-measured SPA-LEED images are distorted at large *k*-values due to non-linearities of the deflection unit used in the SPA-LEED apparatus [120]. The as-

measured images are re-scaled using the known k -values of the diffraction spots obtained in He diffraction. All SPA-LEED images presented here are after re-scaling.

Results and Discussion

A SPA-LEED image recorded at 65 eV electron energy is shown in Figure 3.1, top. The spatial and intensity distribution of the diffraction spots reveals a perfect 10-fold symmetry. The spots which are equidistant from the specular spot (the central brightest spot) have an equal intensity and lie on the corners of a regular decagon. Thus the rotation of the diffraction pattern by $2\pi/10$ around the axis perpendicular to the plane of paper and passing through the specular spot (i.e., the 10-fold axis) transforms it into itself revealing a 10-fold symmetry. The diffraction pattern contains two sets of inequivalent 2-fold axes perpendicular to the 10-fold axis, which appear alternately at every 18° . Detailed studies of the surfaces perpendicular to these two inequivalent 2-fold axes will be presented in the next chapter.

Apart from these 10-fold and 2-fold symmetries, the SPA-LEED image exhibits self-similar patterns. For example, distributions of spots forming pentagons A-A', B-B', and C-C' are self-similar (Figure 3.2). Proper scaling of each pattern produces another. The scaling factor is related by the golden mean τ , which is related to the pentagonal symmetry (the ratio between the center-to-vertex-distance and center-to-mid-edge-distance of a regular pentagon is equal to $\tau/2$). The areas of the pentagons A, B, C, A', B', and C' have the ratio $\tau^4 : \tau^3 : \tau^2 : \tau^2 : \tau^1 : \tau^0$.

The SPA-LEED images (Figures 3.1 and 3.2) display densely distributed spots. The appearance of dense spots is a special feature of quasicrystals. More than 500 diffraction spots have been observed in the range of $k_{\parallel} < 3 \text{ \AA}^{-1}$. Diffraction patterns of non-reconstructed surfaces of periodic crystals would show much fewer spots (only around 20) in this range.

An additional sharp spot is observed very close to the specular (marked by a black square in Figure 3.4). This is the specular spot of a secondary grain present in the sample and not related to the diffraction from the main grain. Few diffraction spots associated with the secondary grain have been observed close to the strong diffraction spots of the main grain.

The diffraction patterns display very sharp spots. The spots are as sharp as those observed in the diffraction patterns of periodic crystal surfaces. The full-width at half-maxima (FWHM) of the specular spot is $\sim 0.02 \text{ \AA}^{-1}$. The corresponding real space dimension of the FWHM is around 300 \AA , which is in the same order of magnitude of the transfer width of the SPA-LEED

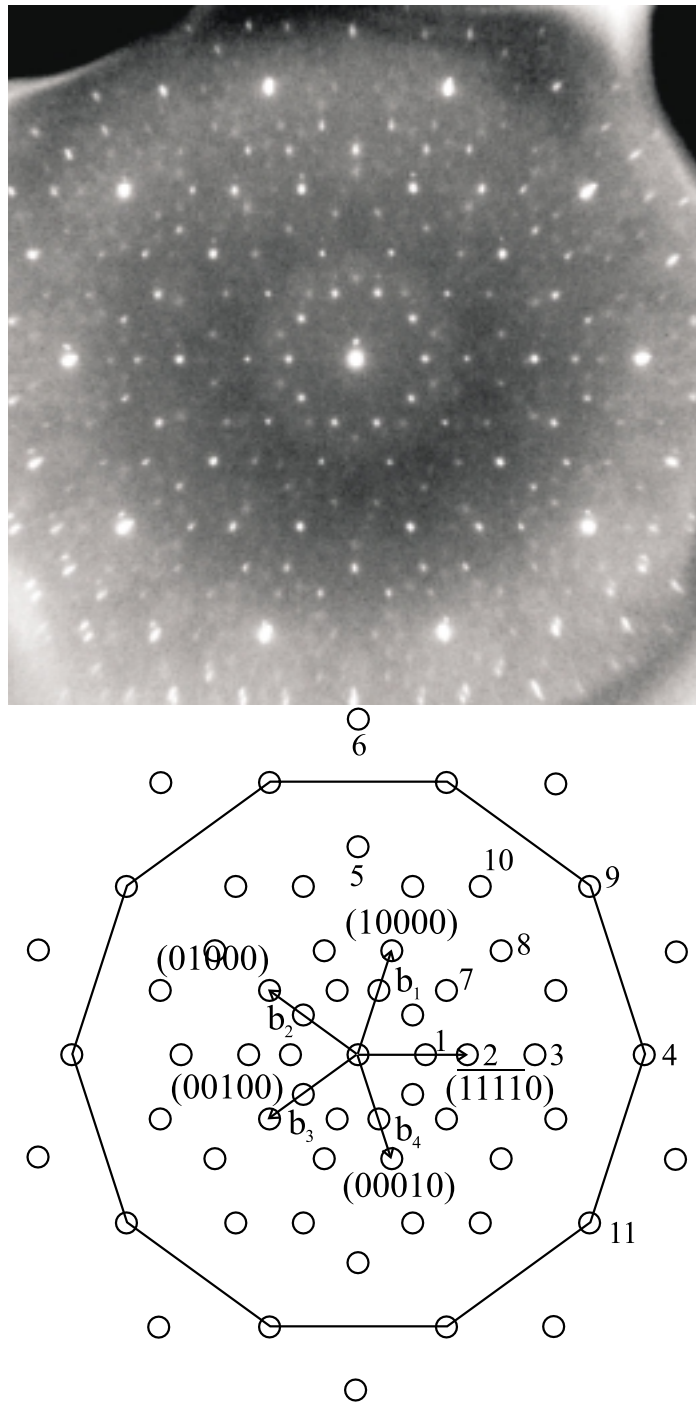


Figure 3.1: A SPA-LEED image (logarithmic gray scale of electron intensity) of the 10-fold surface of d -Al_{71.8}Ni_{14.8}Co_{13.4} recorded at 65 eV electron energy (top). The position of strong spots are shown by circles (bottom). The bulk reciprocal basis vectors $\mathbf{b}_j = b (\cos \frac{2\pi j}{5}, \sin \frac{2\pi j}{5}, 0)$ ($j = 1, \dots, 4$ and $b = 1.02 \text{ \AA}^{-1}$) are used to index the diffraction pattern. The fifth vector $(\bar{1}\bar{1}\bar{1}10)$ is sum of the four vectors \mathbf{b}_j ($j = 1, \dots, 4$) and not an independent basis vector.

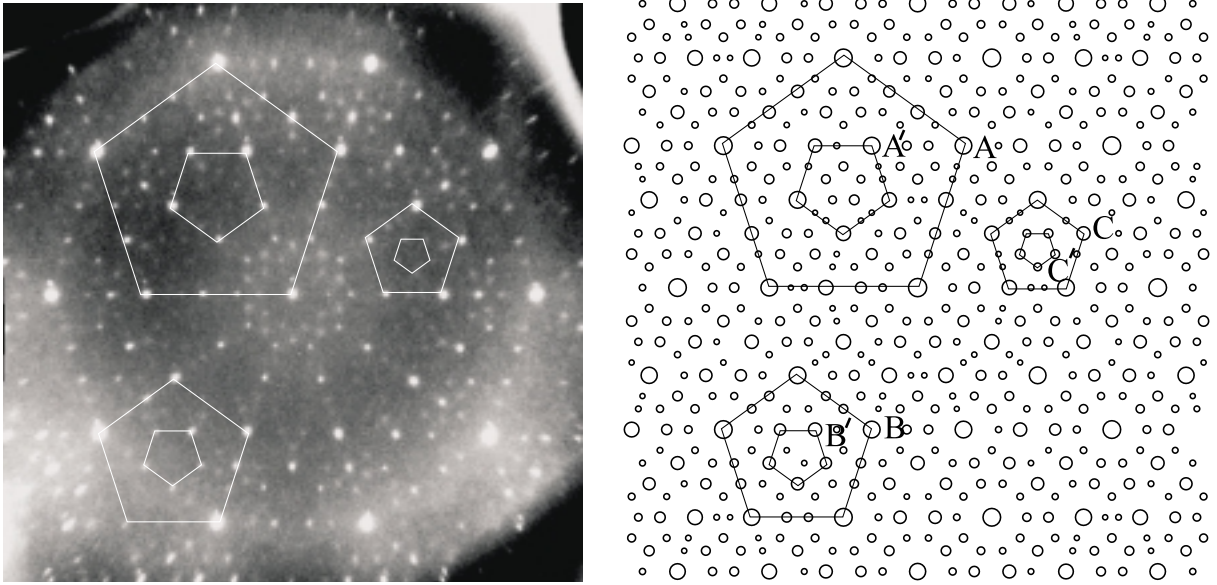


Figure 3.2: A SPA-LEED image (gray scale) of the 10-fold surface of $d\text{-Al}_{71.8}\text{Ni}_{14.8}\text{Co}_{13.4}$ recorded at 75 eV electron energy (left) and the calculated diffraction pattern (right). The pentagons demonstrate self-similar patterns.

instrument. The sharpness of the diffraction spots is evidence of a long range order in the surface region.

Positions of diffraction spots are related by the golden mean, revealing a perfect quasicrystalline ordering. The diffraction vectors of individual spots will be presented later. For the moment, consider the positions of the strong spots marked by circles in Figure 3.1, bottom. The strong spots are on the circles with radii of 0.63 \AA^{-1} , 1.02 \AA^{-1} , 1.65 \AA^{-1} , 1.95 \AA^{-1} , 2.67 \AA^{-1} , and 3.15 \AA^{-1} . The radii are related to each other by $\tau^{-1} : \tau^0 : \tau^1 : \tau\chi : \tau^2 : \tau^2\chi$, where χ is an irrational number and given by $\chi = 2 \sin \frac{\pi}{5} = \sqrt{3 - \tau} = 1.1755 \dots$. As the golden mean, the constant χ is related to the pentagonal geometry. It is equal to edge-to-radius ratio of a regular pentagon.

Five independent vectors \mathbf{b}_j ($j = 1, \dots, 5$) are needed to index the bulk diffraction pattern [40, 64]. Among these five, the four vectors $\mathbf{b}_j = b (\cos \frac{2\pi j}{5}, \sin \frac{2\pi j}{5}, 0)$ ($j = 1, \dots, 4$ and $b = 1.02 \text{ \AA}^{-1}$) are within the quasiperiodic plane and form the basis vector of the reciprocal lattice of the surface. The fifth vector $\mathbf{b}_5 = b_5(0, 0, 1)$ ($b_5 = 0.78 \text{ \AA}^{-1}$) is along the periodic direction (here perpendicular to the plane of paper in the figures) and can be neglected in the discussion of diffraction from the 10-fold surface.

Spots	1	2	3	4	5	6
$(h_1h_2h_3h_4)$	(1001)	$(\bar{1}\bar{1}\bar{1}\bar{1})$	$(0\bar{1}\bar{1}0)$	$(\bar{1}\bar{2}\bar{2}\bar{1})$	$(100\bar{1})$	$(11\bar{1}\bar{1})$
H_{\parallel}^x/b	τ^{-1}	1	τ	τ^2	0	0
$H_{\parallel}^y/b\chi$	0	0	0	0	τ	τ^2
H_{\parallel}/b	τ^{-1}	1	τ	τ^2	$\tau\chi$	$\tau^2\chi$
H_{\parallel}	0.63	1.02	1.65	2.67	1.94	3.14
H_{\perp}^x/b	τ	1	$-\tau^{-1}$	τ^{-2}	0	0
$H_{\perp}^y/b\chi$	0	0	0	0	-1	τ^{-1}
H_{\perp}/b	τ	1	τ^{-1}	τ^{-2}	χ	$\tau^{-1}\chi$
H_{\perp}	1.65	1.02	0.63	0.39	1.2	0.74

Table 3.1: A list of diffraction vectors and Miller indices $(h_1h_2h_3h_4)$ of some strong spots. Spot numbers (S. N.) are given in Figure 3.1. The \mathbf{H}_{\parallel} and \mathbf{H}_{\perp} are decomposed as $\mathbf{H}_{\parallel} = (H_{\parallel}^x, H_{\parallel}^y, 0)$ and $\mathbf{H}_{\perp} = (H_{\perp}^x, H_{\perp}^y)$.

Almost all diffraction spots can be indexed by using the four basis vectors \mathbf{b}_j ($j = 1, \dots, 4$). The four basis vectors are pointing from the center to four of the five corners of a regular pentagon. Since the pentagonal geometry involves the golden mean, the diffraction vectors obtained by linear combination of these basis vectors are related by the golden mean. The diffraction vectors $\mathbf{H}_{\parallel} = \sum_{j=1}^4 h_j \mathbf{b}_j$ and the Miller indices $(h_1h_2h_3h_4)$ of some strong spots are given in Table 3.1. The table demonstrates the τ -relation of diffraction vectors.

In a higher dimension description of decagonal quasicrystals, the basis vectors \mathbf{b}_j ($j = 1, \dots, 5$) are considered as physical space projection of the 5D reciprocal basis vectors. The perpendicular space components of the 5D basis are given by $\mathbf{b}'_j = b (\cos \frac{6\pi j}{5}, \sin \frac{6\pi j}{5})$ ($j = 1, \dots, 4$). The diffraction vectors associated with \mathbf{b}'_j can be calculated by $\mathbf{H}_{\perp} = \sum_{j=1}^4 h_j \mathbf{b}'_j$. Values of \mathbf{H}_{\perp} of some strong spots are shown in Table 3.1. The relation of diffraction intensity with H_{\perp} ($= |\mathbf{H}_{\perp}|$) can be realized from these values. One can see that spots having larger H_{\perp} are weaker or vice versa. For example, the brightest among the observed spots (say the $(10\bar{1}\bar{1})$ spot numbered '4' in Figure 3.1, bottom) have the lowest value of H_{\perp} . This is a very important feature of quasicrystal diffraction patterns, which makes it possible to observe distinct spots as the intensity of spots having very large H_{\perp} are experimentally undetectable.

It is worthwhile to note that there exist other spots brighter than the $(10\bar{1}\bar{1})$ at larger \mathbf{H}_{\parallel} .

The position of these spots can be obtained by adding the diffraction vectors of the observed brightest spots. For example, addition of the diffraction vectors of the spots $(0\bar{1}\bar{2}\bar{1})$ (spot ‘9’) and $(\bar{1}\bar{2}\bar{1}0)$ (spot ‘11’) gives the position of the spot $(\bar{1}\bar{3}\bar{3}\bar{1})$, which has $H_{\perp} = b \tau^{-3} = 0.245 \text{ \AA}^{-1}$ and $H_{\parallel} = b \tau^3 = 4.32 \text{ \AA}^{-1}$. The H_{\perp} value is lower than that of $(110\bar{1})$ or $(0\bar{1}\bar{2}\bar{1})$, and hence should have higher intensity. The H_{\parallel} value is τ times larger than that of $(110\bar{1})$ or $(0\bar{1}\bar{2}\bar{1})$. In principle, a continuous addition of diffraction vectors of brighter spots yields the positions of the maximum possible brightest spots with $H_{\perp} \rightarrow 0$ and very large H_{\parallel} .

Discussed in Section 1.3, clusters of 20 \AA diameter are located at the vertices of a pentagonal Penrose pattern of 20 \AA edge length in the normal phase of the *d*-Al-Ni-Co, while in the superstructure phase the clusters are located at the vertices of a rhombic Penrose of the same edge length [40, 64, 66]. The diffraction pattern of the pentagonal (or rhombic) tiling can be calculated via Fourier transform of the decagonal (or pentagonal) atomic surfaces [5]. The normal phase diffraction pattern is calculated by using the Fourier transform of the decagonal atomic surfaces. The Fourier amplitude versus H_{\perp} is an oscillating function (see Figure 1.11). An envelope function is used to calculate the diffraction pattern in order to avoid the extinction of selected diffraction spots, as the present interest is to find the distribution of all possible diffraction peaks in a general decagonal structure. The resulting diffraction pattern is shown in Figure 3.2, right. A quantitative comparison between the calculated and experimental intensities would not be meaningful because the calculation excludes many factors such as the contribution of individual atoms, multiple scattering, and temperature. However, the calculated diffraction pattern reflects the symmetry of the measured diffraction pattern and provides spot positions. The calculated diffraction pattern superposed on the experimental SPA-LEED data is shown in Figure 3.3. It reveals that almost all diffraction spots are at positions expected from the bulk. Representative of those peaks that cannot be obtained by using the basis \mathbf{b}_j are marked by white circles.

The weak spots marked by white circles in Figure 3.3, 3.5, and 3.6 are identified as superstructure spots. These spots appear around strong diffraction spots forming a decagon (Figure 3.5). The superstructure basis vectors \mathbf{s}_j ($j = 1, \dots, 4$) are rotated by $\frac{\pi}{10}$ with respect to the normal basis vectors \mathbf{b}_j (Figure 3.4). The length s of the superstructure basis vectors is 0.53 \AA^{-1} , which is smaller than b by a factor of $2 \cos \frac{\pi}{10} = \tau\chi$.

The diffraction pattern can be indexed by using the superstructure basis vectors. The

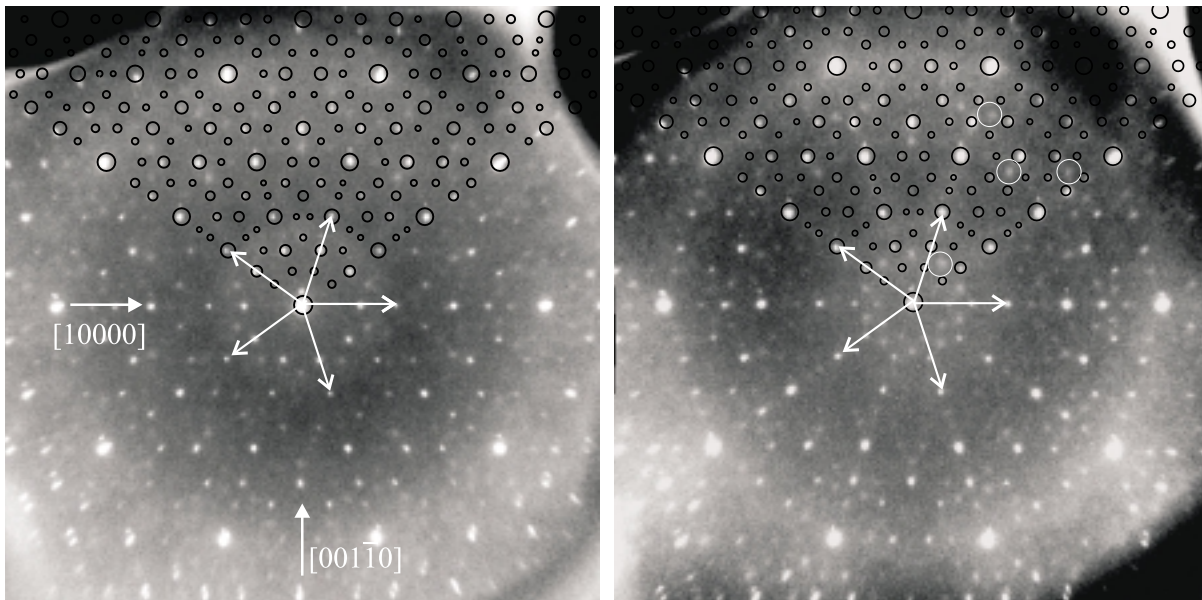


Figure 3.3: A comparison between the calculated and experimental data. SPA-LEED images recorded at 65 eV (left) and 75 eV (right) electron energy. Black circles reflect calculated normal intensities. The area of the circles is proportional to the log of the calculated diffraction intensity. Superstructure spots are encircled by large white circles and the area of the circles is not scaled with intensity.

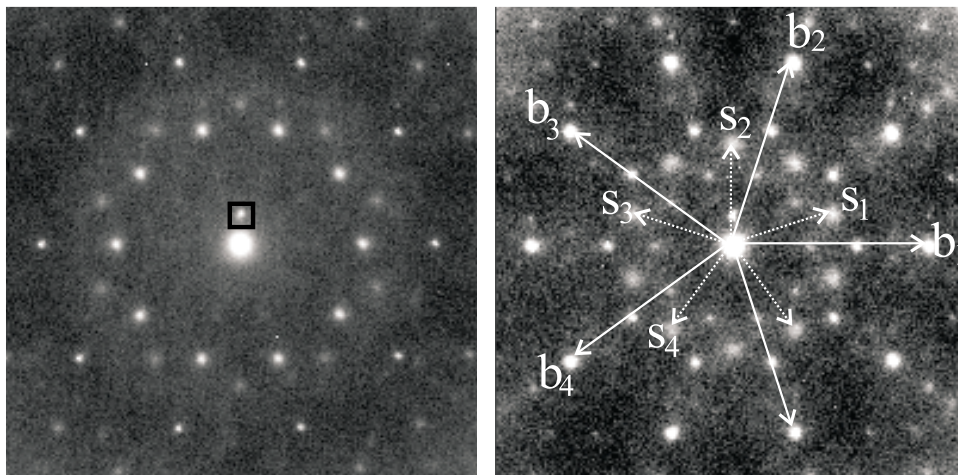


Figure 3.4: SPA-LEED images with magnified scale (left at electron energy of 65 eV and right at 75 eV). The normal structure and the superstructure basis vectors \mathbf{b}_j and \mathbf{s}_j of length 1.02 \AA^{-1} and 0.53 \AA^{-1} are shown as solid and dotted arrows, respectively. The superstructure basis is rotated by $\frac{\pi}{10}$ with respect to the normal basis. The spot very close to the specular (marked by a square) is the specular spot of the secondary grain present in the sample.

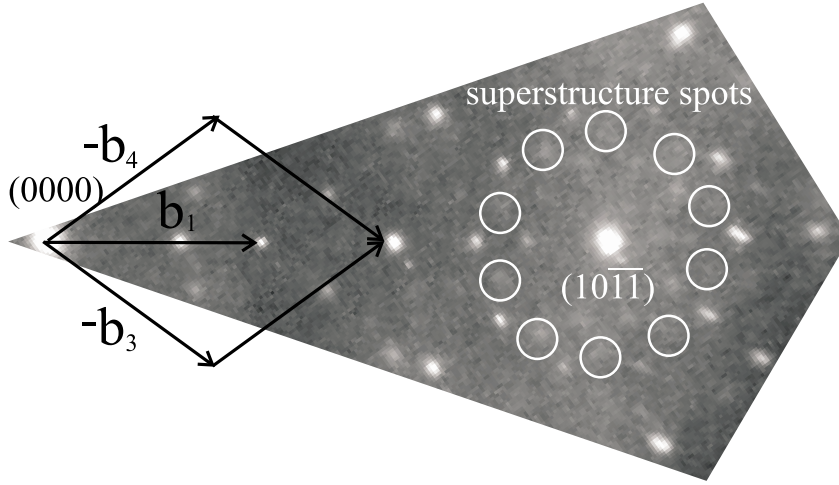


Figure 3.5: Superstructure spots (marked by white circles) appearing around the $10\bar{1}\bar{1}$ spot, one of the strong spots of the normal phase, forming a decagon.

diffraction vectors with respect to the superstructure basis vectors are $\mathbf{H}_{\parallel} = \sum_{j=1}^4 h_j^s \mathbf{s}_j$ with $\mathbf{s}_j = s(\cos \frac{2\pi j}{5}, \sin \frac{2\pi j}{5}, 0)$ and $s = b/(\tau\chi) = 0.53 \text{ \AA}^{-1}$. The perpendicular space components corresponding to these diffraction vectors can be calculated by $\mathbf{H}_{\perp} = \sum_{j=1}^4 h_j^s \mathbf{s}'_j$ with $\mathbf{s}'_j = s'(\cos \frac{6\pi j}{5}, \sin \frac{6\pi j}{5}, 0)$ and $s' = b/2 \cos \frac{3\pi}{10} = b/\chi = s\tau$ [88]. Values of H_{\parallel} , H_{\perp} , and Miller indices ($h_1^s h_2^s h_3^s h_4^s$) of some spots are presented in Table 3.2.

The type of a diffraction spot is given by the sum $n = \sum_i h_i^s$. Spots with n a multiple of 5 are normal structure spots, while those with $n = 5m \pm 1$ and $n = 5m \pm 2$, with integer m are referred to as S1 and S2, respectively. All detected superstructure spots satisfy $\sum_i h_i^s = 5m \pm 1$ (see Table 3.2), and hence are identified as S1 spots.

The bulk structure of $d\text{-Al}_{71.8}\text{Ni}_{14.8}\text{Co}_{13.4}$ possesses type I superstructure at room temperature. Thus, one should expect both S1 and S2 spots in the diffraction pattern of the bulk terminated surface. However, only S1 spots were observed. This may not be so surprising. As predicted by theoretical calculations [91] and also revealed by X-ray diffraction data [88], S2 spots are even weaker than the S1 spots. The observed S1 spots are already extremely weak. Therefore, the intensities of S2 spots are likely below detection limit.

The position of the $(0\bar{2}\bar{3}\bar{2})$ spot, which is one of the S2 spots, is marked by white square in Figure 3.6. No intensity has been observed at this position even though it is one of the brighter S2 spots as expected from its H_{\perp} value. The H_{\perp} value of the spot is 0.20 \AA^{-1} , which is much lower than that of the observed brightest normal spots.

The superstructure spots take fractional indices with respect to the normal basis vectors.

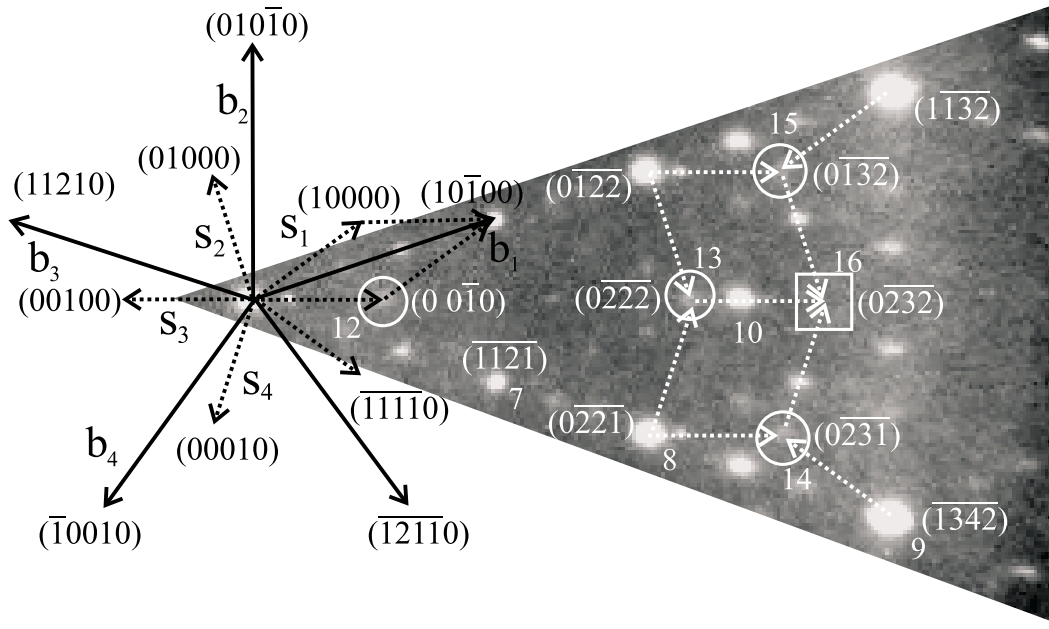


Figure 3.6: Indexing of diffraction spots by using the superstructure basis. The spots with $n = \sum_i h_i^s$ a multiple of 5 are normal structure spots, while those with $n = 5m \pm 1$, with integer m are the S1 spots. Position of a S2 spot satisfying $n = 5m \pm 2$ is marked by a white square.

The superstructure basis can be obtained from the normal basis by $\mathbf{s}_j = \sum_i S_{ij}^{-1} \mathbf{b}_i$ with,

$$S^{-1} = \frac{1}{5} \begin{bmatrix} 2 & -1 & 1 & -2 \\ 2 & 4 & 1 & 3 \\ -3 & -1 & 1 & -2 \\ 2 & -1 & 1 & 3 \end{bmatrix}. \quad (3.1)$$

Because of the presence of the $\frac{1}{5}$ fraction term in the matrix, the superstructure spots indexed with respect to normal basis vectors take $\frac{1}{5}$ -integer indices (see Table 3.2).

Line scans along the $[10000]$ and $[001\bar{1}0]$ directions at electron energies of 65 eV and 75 eV are shown in Figure 3.7. For scans along the $[10000]$ -azimuth, the peaks are at 0.39 \AA^{-1} , 0.63 \AA^{-1} , 1.02 \AA^{-1} , 1.26 \AA^{-1} , 1.40 \AA^{-1} , 1.65 \AA^{-1} , 2.04 \AA^{-1} , 2.28 \AA^{-1} , and 2.67 \AA^{-1} . The peak positions can be obtained by $\Delta k_{\parallel} = k_0(m + n\tau)$, with $k_0 = 1.02 \text{ \AA}^{-1}$ and $(m, n) = (2, \bar{1})$, $(\bar{1}, 1)$, $(1, 0)$, $(\bar{2}, 2)$, $(3, \bar{1})$, $(0, 1)$, $(2, 0)$, $(\bar{1}, 2)$, and $(1, 1)$, respectively. Similarly, for scans along the $[001\bar{1}0]$ -azimuth, the peak positions are related by $\Delta k_{\parallel} = k_0 \chi \tau (m + n\tau) = 1.94(m + n\tau) \text{ \AA}^{-1}$ with $(m, n) = (\bar{1}, 1)$ and $(1, 0)$, respectively. The superstructure peaks are at 0.53 \AA^{-1} and 1.7 \AA^{-1} and related by $\Delta k_{\parallel} = (k_0/\chi\tau)(m + n\tau) = 0.53(m + n\tau) \text{ \AA}^{-1}$ with $(m, n) = (1, 0)$ and

Spots	$(h_1 h_2 h_3 h_4)$	$(h_1^s h_2^s h_3^s h_4^s)$	$n = \sum_i h_i^s \pm 5m$	Type	$ \mathbf{H}_{\parallel} /\text{\AA}^{-1}$	$ \mathbf{H}_{\perp} /\text{\AA}^{-1}$
7	$(00\bar{1}0)$	$(\bar{1}\bar{1}\bar{2}\bar{1})$	0	N	1.02	1.02
8	$(0\bar{1}\bar{1}\bar{1})$	$(0\bar{2}\bar{2}\bar{1})$	0	N	1.65	0.63
9	$(0\bar{1}\bar{2}\bar{1})$	$(\bar{1}\bar{3}\bar{4}\bar{2})$	0	N	2.67	0.39
12	$\frac{1}{5}(31\bar{1}2)$	$(00\bar{1}0)$	-1	S1	0.53	0.87
13	$\frac{1}{5}(\bar{2}\bar{4}\bar{6}\bar{6})$	$(0\bar{2}\bar{2}\bar{2})$	-1	S1	1.73	1.07
14	$\frac{1}{5}(\bar{3}\bar{4}\bar{6}\bar{3})$	$(0\bar{2}\bar{3}\bar{1})$	-1	S1	2.16	0.71
15	$\frac{1}{5}(31\bar{6}\bar{3})$	$(0\bar{1}\bar{3}\bar{2})$	-1	S1	2.16	0.71
16	$\frac{1}{5}(1\bar{3}\bar{7}\bar{6})$	$(0\bar{2}\bar{3}\bar{2})$	-2	S2	2.27	0.20

Table 3.2: List of diffraction vectors and Miller indices: $(h_1^s h_2^s h_3^s h_4^s)$ are the Miller indices with respect to the superstructure basis, while $(h_1 h_2 h_3 h_4)$ with respect to the normal basis. (N: normal spots, S1: S1 superstructure spots, and S2: S2 superstructure spots. See Figure 3.6 for spot numbering.)

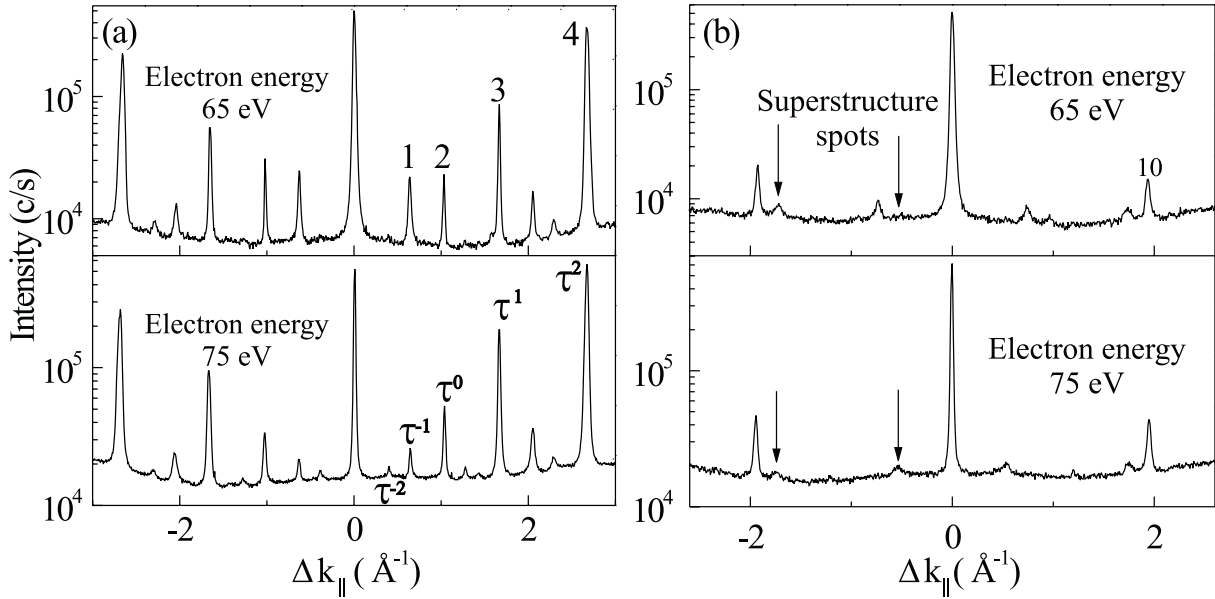


Figure 3.7: Line scans along the $[10000]$ (a) and $[001\bar{1}0]$ (b) azimuth. The position of strong spots along $[10000]$ show a ratio of $\tau^{-2} : \tau^{-1} : \tau^0 : \tau^1 : \tau^2$. The peak numbers correspond to the diffraction spots numbered in Figure 3.1. The superstructure peaks are indicated by arrows.

(0,2). The fact that the positions of the superstructure peaks are related by the golden mean indicates a quasicrystalline superlattice ordering in the surface region. The superstructure spots are found to broaden. The FWHM of the spots is almost five times larger than that of the specular peak and three times that of the higher order diffraction peaks. This indicates a short range correlation of atoms associated with the superstructure ordering.

A comparison of line scans at 65 eV and 75 eV shows a strong variation in diffraction intensity over a relatively small energy range. For example, clearly observed superstructure peaks at 0.53 \AA^{-1} at 75 eV cannot be seen at 65 eV.

3.2 Helium Atom Scattering

Surface Preparation

Again, the surface was prepared by sputtering and annealing. A suitable sputter-annealing condition was obtained after several trials. It was found that the surface prepared by two or three cycles of sputtering (Ne^+ , 1 keV, $3 \mu\text{A}$, for 30 minutes) and annealing (600-850 °C for 30 minutes) is clean enough for the first observation of LEED. However, further cleaning cycles are needed to observe He diffraction with intense peaks because the extreme surface sensitivity of He atom scattering necessitates a high perfection of the surface. The quality of the surface was examined after each sputter-annealing cycle by monitoring the He specular intensity. The cleaning processes were repeated until an optimum He specular intensity was obtained. The clean surface was found to contaminate within a few hours at the prevailing UHV conditions with a base pressure of 2×10^{10} mbar. Annealing the contaminated surface at 600-850 °C for a few minutes recovers the surface quality to within a few percent in the specular intensity.

Results and Discussion

The two inequivalent high symmetry directions of the 10-fold surface can be represented by $[10000]$ and $[001\bar{1}0]$ (see Figure 3.3). Helium diffraction from the clean surface was measured along these high symmetry directions at different beam energies from 9 meV to 44 meV. The spectra for selected beam energies are shown in Figure 3.8. The specular intensity is dominant for all energies. Its intensity of 10^5 c/s is comparable to the specular intensity of high quality cleaved surfaces of e.g., $\text{MgO}(001)$ [125] and $\text{GaAs}(110)$ [126]. Due to their high scattering cross

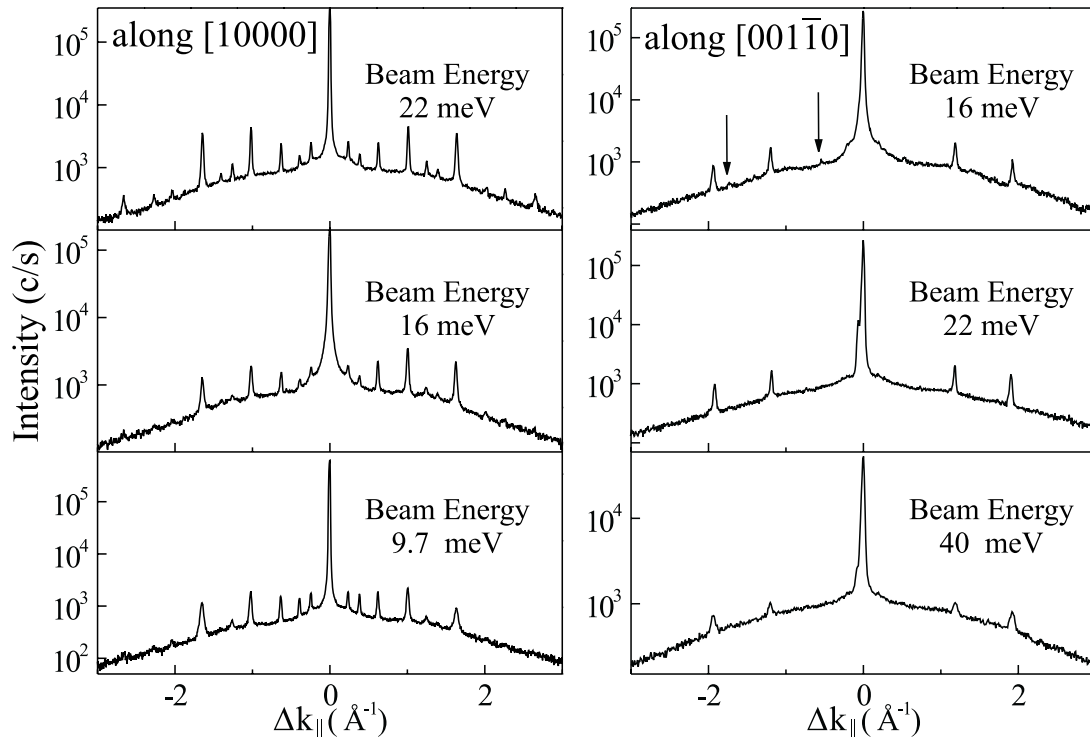


Figure 3.8: He diffraction along $[10000]$ (left) and $[001\bar{1}0]$ (right) at different beam energies. Superstructure peaks are indicated by arrows.

section, adsorbates and vacancies can be detected in the 0.001 monolayer range by a significant reduction of the specular He atom intensity [92]. The observation of such a high specular intensity therefore indicates an extremely low density of defects.

The surface corrugation can be determined from the intensity distribution of the diffraction spots [92]. A higher corrugation causes more He atoms to be scattered into diffraction peaks at higher momentum transfer. As the specular peak in the observed spectra dominates the diffraction pattern (other diffraction peaks have two orders of magnitude lower intensity) a very low corrugation can be inferred.

HAS and SPA-LEED of the 10-fold surface are compared in Figure 3.9. HAS and SPA-LEED have different surface sensitivity. While HAS gives exclusive information of the topmost surface layer as the electron density extending out of the solid reflects the He atoms well above the surface [92]. In contrast, electrons penetrate several Angstroms into the surface before being scattered from the atom potential and hence provides information from a few topmost layers (refer to Chapter 2 for a more detail explanation). The comparison shows identical peak

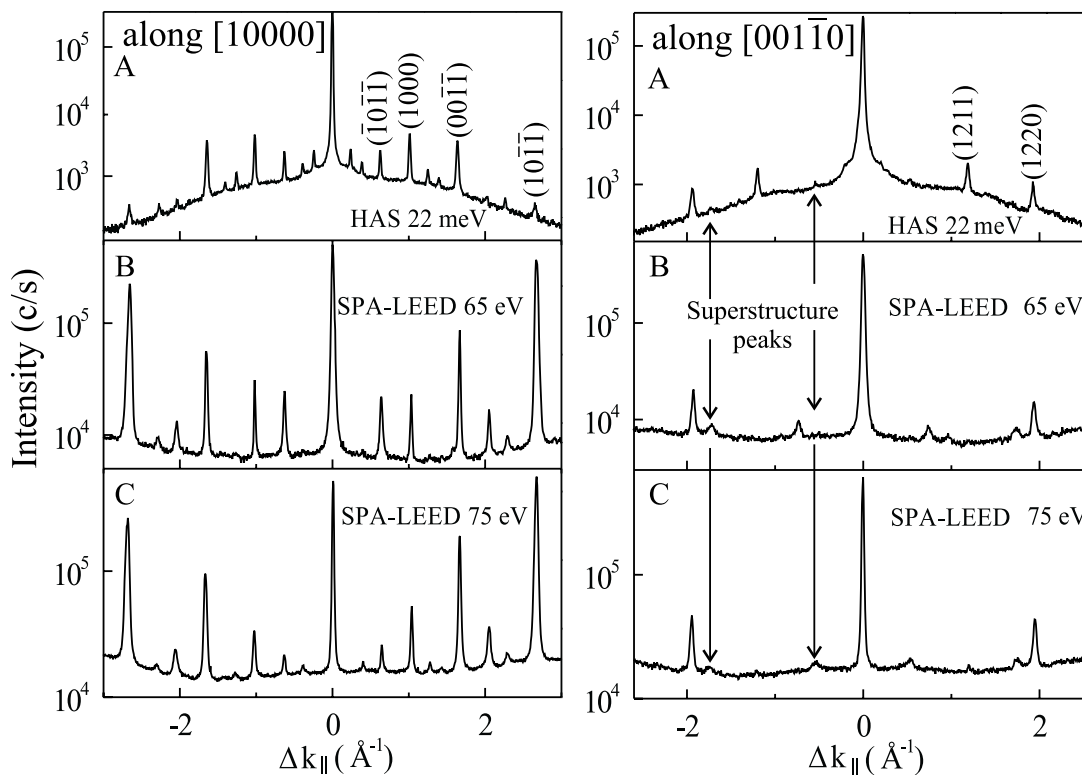


Figure 3.9: A comparison between HAS and SPA-LEED along [10000] (left) and [001 $\bar{1}$ 0] (right). Spectrum ‘A’ is He diffraction and ‘B’ and ‘C’ are SPA-LEED at 65 eV and 75 eV, respectively. The indexing follows Section 3.1.

positions in He diffraction and SPA-LEED. As the spot positions of SPA-LEED can be explained by the bulk reciprocal basis vectors (see previous section), the observation of the identical peak positions in HAS and SPA-LEED reveals that the topmost surface layer has an identical order as the bulk.

As observed in SPA-LEED, He diffraction also shows only S1 spots with very weak intensity (see comparison in Figure 3.9, right). The appearance of these peaks is very sensitive to sample alignment and the quality of the surface due to the extremely weak intensity.

Helium diffraction from the surface prepared under different conditions is compared in Figure 3.10. The lower spectrum was from the surface annealed at 600-650 °C. The sample was mounted on an Ohmic heater. In contrast, the upper spectrum was taken from the surface annealed by using an electron beam (e-beam) heater. With this e-beam heater, the sample could be annealed at higher temperatures. For the particular spectrum shown in the figure, the sample

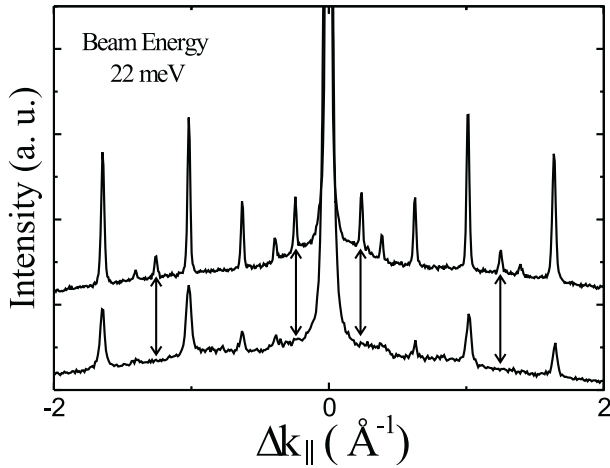


Figure 3.10: A comparison of He diffraction along [10000] from differently prepared surfaces. The upper and spectra were taken from the surface annealed at 800-850 °C and 600-650 °C (sputtering: 5-20 μA , 30 minutes in both case), respectively. The intensity of the lower spectrum has been multiplied by a factor of 1.5.

was annealed at 800-850 °C. A difference between the two heating systems is that the cooling rate of the sample after annealing stopped is slower in the case of the Ohmic heater as compared to the e-beam heater.

As seen in the figure, the two spectra are qualitatively different (note that the intensity of the lower spectrum has been multiplied by a factor of 1.5 to equalize the background intensity of the two spectra. The asymmetric distribution of the intensity to the left and right of the specular is due to the sample alignment). In the case of higher annealing temperature, more peaks are resolved (for example, peaks at 0.24 \AA^{-1} and 1.26 \AA^{-1} , marked by arrows, are visible only in the upper spectrum) and the observed peaks are more intense. Despite these differences, the peak width is limited by the instrumental resolution in both cases. The width is a measure of a correlation length of quasicrystalline order of the atoms. The sharp peaks imply a long range order in the surface within the length scale of the instrumental transfer width. These observations demonstrate that a quasiperiodic long range order is achieved even with the lower annealing temperature. However, to get a highly ordered surface the higher annealing temperature is needed.

With this superior high temperature preparation, surface phonons have been successfully measured, which will be presented in Chapter 5. Attempts to measure phonons from the surface prepared at lower annealing temperature with the Ohmic heater were unsuccessful. In addition to the structure, the surface morphology is also found to be different for the two surface preparations.

The surface morphology was studied by recording the specular intensity as a function of

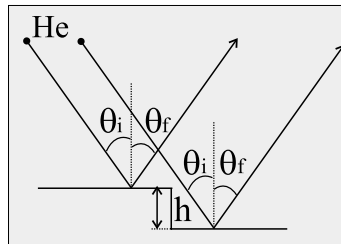
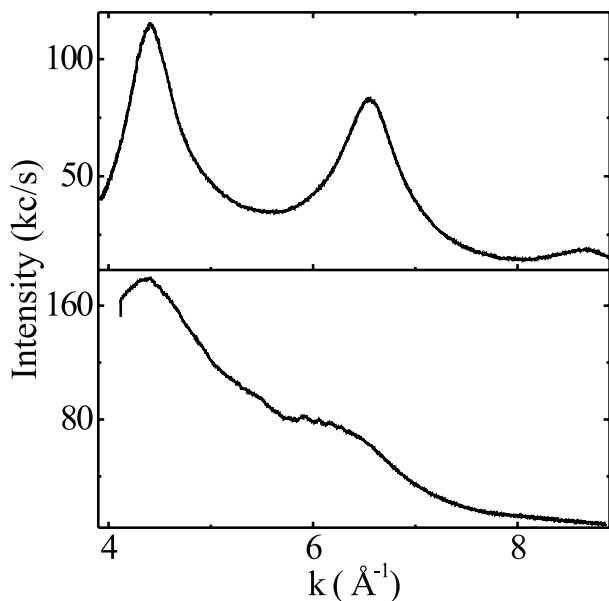


Figure 3.11: He specular intensity as a function of momentum transfer (top: surface prepared with slow cooling; and bottom: surface prepared with fast cooling). The right panel shows a sketch of scattering from two adjacent terraces.

beam energy. Since the parallel momentum transfer during scattering is zero for the specular peak, changes in the beam energy varies only the perpendicular momentum transfer. Note that the parallel momentum transfer Δk_{\parallel} is given by $\Delta k_{\parallel} = k_i(\sin \theta_f - \sin \theta_i)$ with $k_i/\text{\AA}^{-1} = 1.39\sqrt{E_i/m\text{eV}}$ and E_i the He beam kinetic energy. For the specular peak, θ_i is equal to θ_f which yields $\Delta k_{\parallel} = 0$. The specular intensity variation with beam energy thus reflects the vertical roughness of the surface.

Figure 3.11 shows the specular intensity as a function of wavevector k_i . The upper spectrum shows an oscillation due to constructive and destructive interference of the wave scattering from adjacent terraces (see the right panel of the figure). The oscillating period is $\delta k = 2.15 \pm 0.06 \text{ \AA}^{-1}$. From this period, the step height h is calculated to be $h = 2.06 \pm 0.06 \text{ \AA}$ by applying a simple formula $2h \sin \theta_i = 2\pi/\delta k$. The observed height corresponds to the distance between the quasiperiodic planes [64, 66].

The ratio of in-phase and out-of-phase intensity is related to the ratio of the average terrace width and the transfer width of the apparatus [127]. The strong oscillation of the specular intensity is possible only when the terrace width is in the order of the transfer width of the apparatus (about 100 \AA) or less. This morphological information is confirmed by low temperature STM results given in the next section.

The upper and lower spectra in Figure 3.11 were taken from the surface prepared under

different conditions (the preparation condition is identical to that explained above). The lower spectrum is from the surface obtained by higher temperature e-beam heating based preparation, while the upper was annealed with the Ohmic heater. The lower spectrum shows much weaker oscillations implying that the terrace widths are significantly larger. STM investigation of d -Al₇₂Ni₁₁Co₁₇ also show wider terraces on the surface prepared at higher annealing temperature than in the surface annealed at lower temperature [20].

3.3 Scanning Tunneling Microscopy

Experiment

With a better understanding of surface preparation and surface structure gained from the diffraction data, the surface was investigated by low temperature scanning tunneling microscopy (LT-STM). Measurements were performed in a home-built LT-STM (see Ref. [128] for a description of apparatus details). Since the microscope is completely surrounded by a radiation shield at 4 K, the residual gases of the chamber are trapped on it providing an excellent low background pressure reducing the rate of surface contamination by several orders of magnitude compared to the HAS and SPA-LEED experiments. Once a clean surface was attained the experiments could be continued for three weeks without any significant degradation of surface quality.

All STM images presented here were taken in constant current mode at 6 K. The surface was prepared by sputtering (1.5 kV, 4-10 μ A, for 15-30 minutes) and annealing (650 °C, for 15-20 minutes followed by 700 °C for a few seconds, Ohmic heater).

Results and Discussion

A large scale STM image of the clean surface is shown in Figure 3.12 demonstrating a high density of 2 Å high steps. From various scanned images, an average terrace width of about 100 Å is determined. The terraces are atomically flat with a corrugation of a few tenths of an Angstrom. The steps height and terraces width are in good agreement with the previous observation by HAS. Steps are found to be very rough and are not orientated along any preferential direction. Other decagonal systems (for example, d -Al-Cu-Co [17] and d -Al-Ni-Co with different composition than our sample [18]) also show rough steps.

As shown in Figure 3.13 two types of surface terminations are apparent on a single terrace.

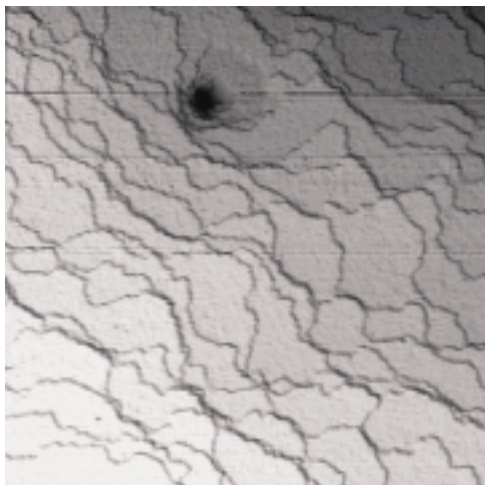


Figure 3.12: A STM image demonstrating a high density of steps ($A = 2110 \times 2110 \text{ \AA}^2$, $V = 1.46 \text{ V}$ and $I = 0.55 \text{ nA}$). Terraces are of approx. 100 \AA and rough steps are observed.

With the same tip and sample condition, some portions of the terrace display more resolved structure (a fine structure) than the other part of the terrace (a coarse structure). The fine structure is imaged slightly lower ($0.2\text{-}0.3 \text{ \AA}$) with respect to the coarse structure. The observation of the two types of structure in a single terrace gives further evidence for the dependence of surface termination on preparation and annealing temperature. Since the coarse structure is dominating the observed data, it will be analysed in more detail in the following.

As introduced in Section 1.3.3, *d*-Al-Ni-Co consists of an alternating stacking of two types of quasiperiodic planes (A and B). The clusters, main building blocks of the system, in each layer have 5-fold symmetry and have the same orientation in a single layer (details about the clusters are discussed later in this section). The orientation of the clusters in layers ‘A’ and ‘B’ are related by inversion symmetry. This is demonstrated by the STM image of two adjacent terraces in

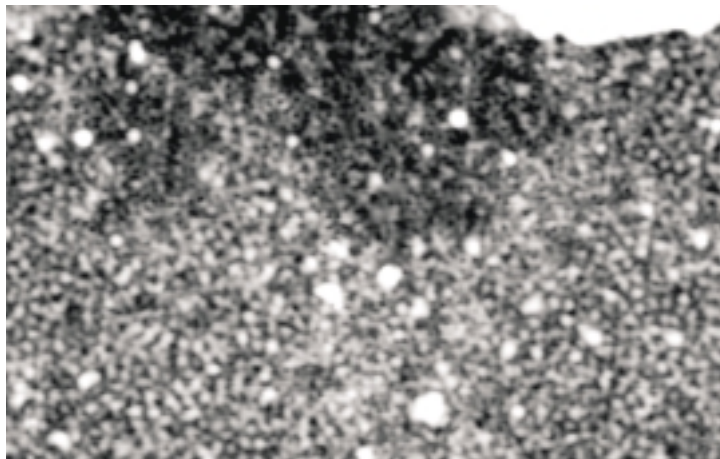


Figure 3.13: A STM image showing two different surface terminations within a single terrace ($A = 290 \times 200 \text{ \AA}^2$, $V = 0.06 \text{ V}$ and $I = 1.4 \text{ nA}$).

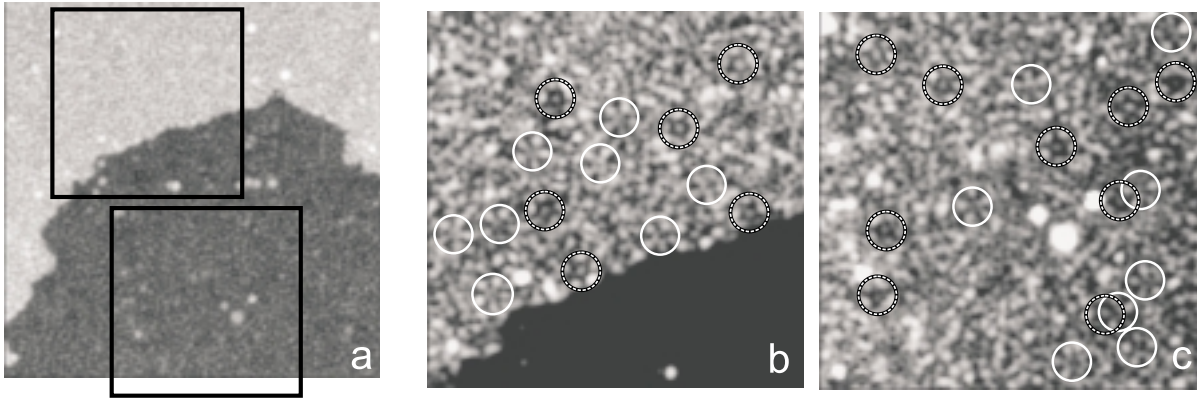


Figure 3.14: A STM image of two adjacent terraces (a) ($A = 316 \times 316 \text{ \AA}^2$, $V = 0.73 \text{ V}$ and $I = 1.5 \text{ nA}$). High resolution images of the areas marked by frames (b and c) ($A = 157 \times 157 \text{ \AA}^2$, $V = 0.73 \text{ V}$ and $I = 1.5 \text{ nA}$). The dotted and full circles marked the two different types of pentagonal-shape feature.

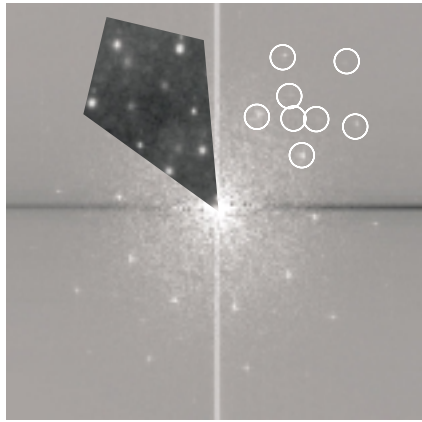


Figure 3.15: A gray scale image of the Fourier transform of the STM image shown in Figure 3.14(a) displaying a 10-fold symmetry with sharp spots. Some of the spots are marked by white circles. Superimposed is a SPA-LEED image taken at 65 eV electron energy.

Figure 3.14(a). High resolution images of the upper and lower terrace are also displayed in Figure 3.14(b-c). The terraces shows two different types of pentagonal-shape features indicated by full and dashed circles. The pentagonal features have the same orientation in a single terrace, but they are in opposite orientation with respect to those in the adjacent terrace.

Gray scale image of the Fourier transform of the image shown in Figure 3.14(a) have a 10-fold symmetry (Figure 3.15). The spots are sharp and are on five rings of radii 1.02 \AA^{-1} , 1.2 \AA^{-1} , 1.35 \AA^{-1} , 1.65 \AA^{-1} , and 1.95 \AA^{-1} within experimental errors. The radii have ratios of $1 : \chi : 3(\tau - \chi) : \tau : \chi\tau$. The position of the spots reveals a long range, quasiperiodic order. The real space value corresponding to the wavevector of the outermost spot ($k = 1.95 \text{ \AA}^{-1}$) is $\sim 3 \text{ \AA}$, which is larger than the length scale expected in an atomically resolved images. The

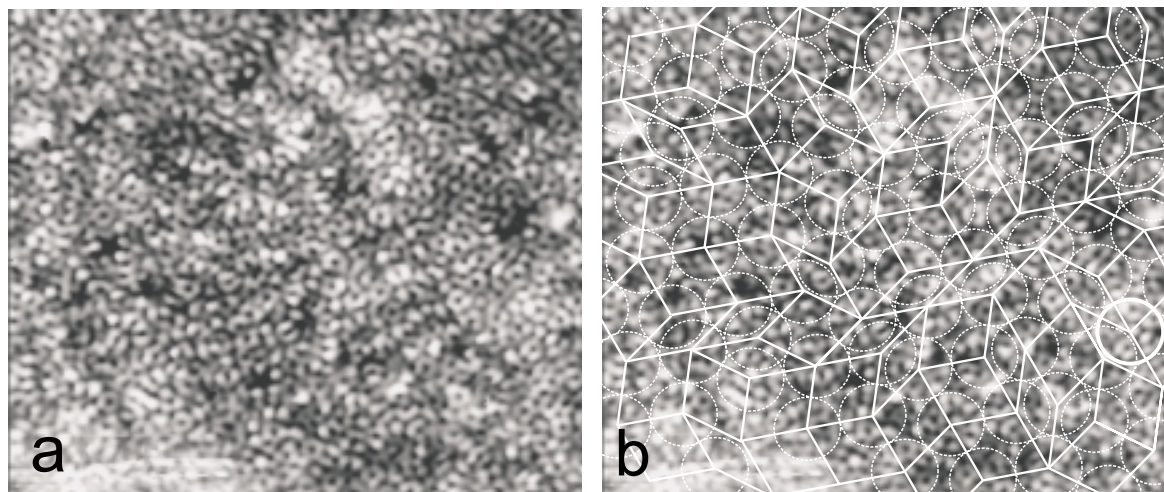


Figure 3.16: A high resolution STM image (a) ($A = 150 \times 115 \text{ \AA}^2$, $V = 0.025 \text{ V}$ and $I = 5 \text{ nA}$) with a tiling overlaid (b).

observed resolution is similar to previous reports on the 10-fold surface of *d*-Al-Ni-Co [18] and *d*-Al-Co-Cu [17]. A portion of a SPA-LEED image is superimposed on the the gray scale image demonstrating that the Fourier transform of the STM image agrees with the SPA-LEED results.

In addition to information about the steps and terraces, more insight of the atomic structure of the surface has been gained. Theoretical structure models of *d*-Al-Ni-Co are based on 20 \AA diameter clusters located at the vertices of a rhombic tiling [64, 66]. In agreement with these bulk structural models, a high resolution image of a portion of a terrace can be overlaid by a rhombic tiling of 20 \AA edge length (Figure 3.16(b)). The vertices of the tiling are located at the centers of cluster indicated by circles in the figure. It should be mentioned that to identify the vertices of the tiling in STM images is not as easy as in the case of transmission electron microscopy (TEM) giving an image of projected structure. In TEM images, the 10-fold symmetric contrast of the columnar clusters are apparent while the STM images (where only the topmost layer is imaged) lack these clear features (see Figure 3.17 for the atoms in the topmost layer of bulk terminated surface and compare it to the projected structure in Figure 1.10). By a careful and intensive search, a tiling was found in one selected high resolution STM image.

Magnified sections of this image are shown in Figure 3.18, left, displaying the two different tiles observed. These are the skinny (with an angle of 36°) and fat (with an angle of 72°) rhombi

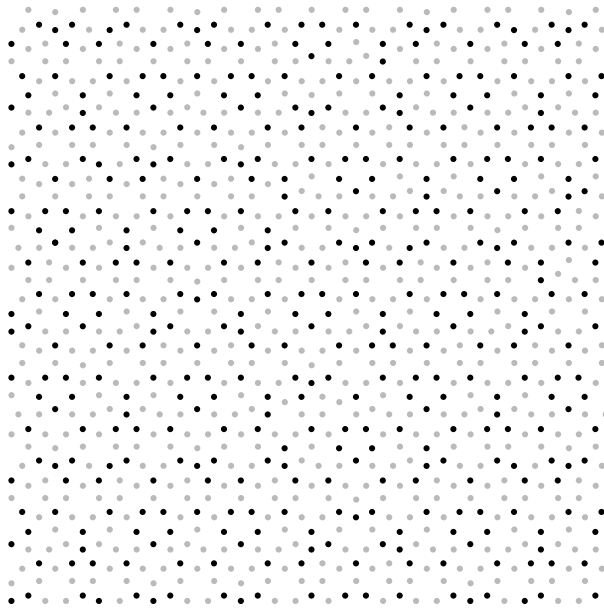


Figure 3.17: The atomic structure on the topmost layer of the bulk terminated surface perpendicular to the 10-fold axis [66]. The dark and gray circles represent transition metals and Al, respectively. For the stacking of the first and second layer of the same area see Figure 1.10.

of a Penrose pattern (Section 1.1.1). The neighboring two clusters are packed in two ways in these rhombi. In one case, they overlap with each other such that the center-to-center distance S is equal to the shorter diagonal of the skinny rhombus. In the second case, they touch head-to-head with center-to-center distance equal to the edge length of the rhombi ($L = S \tau \sim 20 \text{ \AA}$).

The overlaid tiling of Figure 3.16(b) is illustrated in Figure 3.18, right. The tiling does not

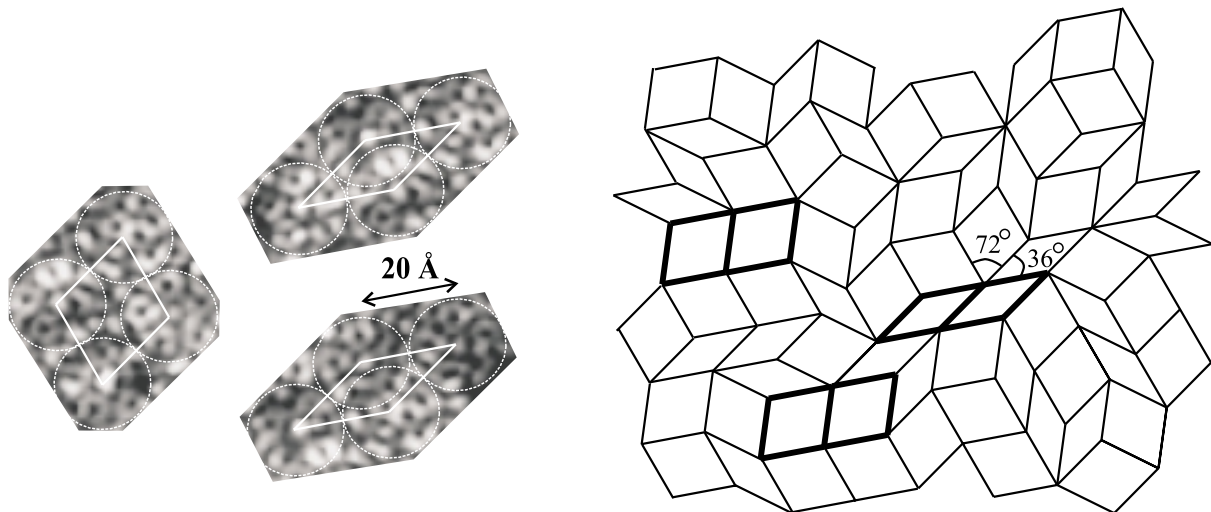


Figure 3.18: Selected magnified sections of the image showing the two different tiles (a) and the observed tiling (b).

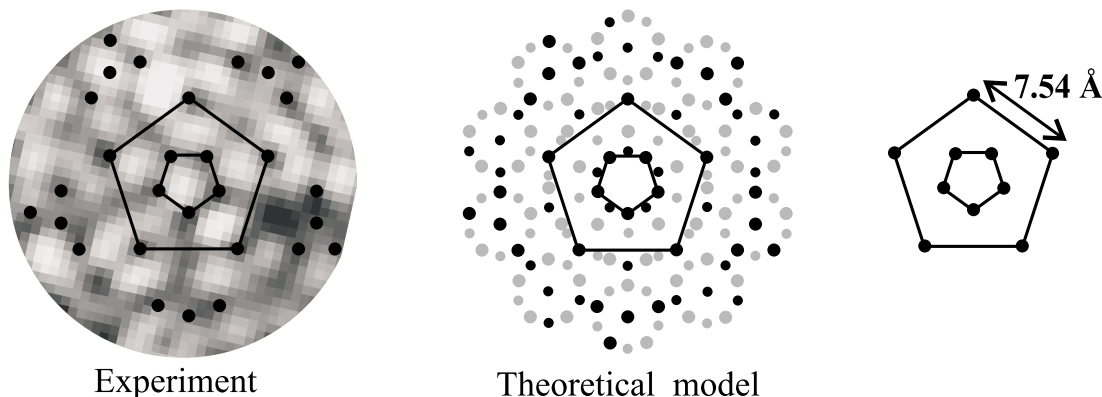


Figure 3.19: A comparison between the observed and theoretical cluster. The observed cluster (left) (the displayed is the magnified cluster marked by bold circle in Figure 3.16(b) and slightly rotated with respect to the original position) and the cluster of theoretical model proposed by Yamamoto *et al.* [66] (middle). Transition metals of the topmost layer in inner first and second rings are indicated by pentagons with the atomic distance of the theoretical model (right).

reflect a section of a perfect rhombic Penrose tiling but is randomized. (Note that the tiling is slightly distorted to accommodate the slight distortion in the STM imaging). A few examples of local arrangements of tiles which are not allowed in a perfect rhombic Penrose tiling are indicated by bold edges in Figure 3.16(d). As outlined in Section 1.3, transmission electron microscopy (TEM) shows that the atomic structure of the type I superstructure phase of Al-Ni-Co can be explained in terms of a random tiling. Since our sample belongs to this phase, the observed tiling thus agrees with the TEM results. A random tiling is believed to be responsible for an entropic stabilization of quasicrystal (Section 1.2). The randomness can be viewed as phason disorder.

The atomic distribution in a cluster of the bulk terminated surface is shown in Figure 3.19. The large and small solid circles represent atoms of the topmost and the second layer, while the dark and gray circles denote transition metals and Al, respectively. The atoms in each layer are arranged in a pentagonal symmetry and the whole atomic arrangement of the first layer is rotated by 36° with respect to that of second layer giving an overall 10-fold symmetry. Agreeing with the bulk terminated surface, the observed clusters show pentagonal symmetry (see an individual cluster in Figure 3.19, left). The dark areas in the cluster (where the tip approaches the sample

to keep the tunneling current constant) seem to be correlated to transition metal sites in the top layer (marked by large dark circles in the cluster), while brighter parts are related to Al. However, the center part of the cluster does not agree with the theoretical model. The observed cluster suggests extra Al atoms to be at the cluster center.

Summary

To summarize this chapter, SPA-LEED images of the surface show very sharp diffraction spots revealing a perfect long range order in the surface region. With the high resolution and high dynamic range of the SPA-LEED apparatus, the observation of nearly 500 diffraction spots in the k -vector range up to 3 \AA^{-1} is possible. The diffraction spots can be indexed by using the bulk decagonal reciprocal basis vectors which implies that the surface preserves the perfect quasicrystalline order of the bulk.

The He specular intensity is comparable to the specular intensity of high quality cleaved surfaces of crystalline systems revealing an extremely low density of defects. He diffraction shows a very low corrugation as the specular intensity dominates the diffraction peaks. A comparison of He diffraction with electron diffraction shows the diffraction peaks are equally observed in both cases giving evidence that the topmost surface layer also retains the perfect quasicrystalline order of the bulk.

Aside from the bulk derived symmetry and order, the surface shows the superstructure of the bulk. The $d\text{-Al}_{71.8}\text{Ni}_{14.8}\text{Co}_{13.4}$ is a type I superstructure phase possessing bulk S1 and S2 superstructure spots. Both He and electron diffraction show very weak S1 spots. The S2 spots are not detected most likely due to their extremely low intensity.

In addition to the structural information, insights into the surface morphology were gained. The specular intensity as a function of momentum transfer shows an oscillation with a period corresponding to a 2 \AA step height. This step height corresponds to the interlayer distance of $d\text{-Al-Ni-Co}$. The average terrace width is estimated to be on the order of 100 \AA .

Low temperature STM (6 K) shows a high density of steps with monoatomic 2 \AA height confirming the morphological features observed in He diffraction. The steps are found to be very rough. Terraces are atomically flat with an average width of 100 \AA . The terraces show 5-fold symmetric motives, which have identical orientation in a single terrace but are oppositely oriented in successive terraces confirming the alternating stacking of two types of quasiperiodic

planes. Fourier transforms of the structure on single terraces yield sharp spots with a 10-fold symmetry demonstrating the long range quasiperiodic order. The Fourier transform is in good agreement with the SPA-LEED images of the same surface.

Clusters of 20 Å diameter located at the vertices of a rhombic tiling have been identified. The tiling deviates from a perfect rhombic Penrose tiling in agreement with the transmission electron microscopy of the type I superstructure phase, which found the structure of this phase characterized by a random rhombic tiling.

Comparing different surface preparations, a dependence of surface termination and morphology on the annealing temperature was observed. Helium diffraction from the surface prepared at higher annealing temperature shows more intense peaks as compared to the surface prepared at lower annealing temperature. This demonstrates that annealing at higher temperature yields a more ordered structure. This observation is confirmed by low temperature STM. The STM images of the surface prepared at lower annealing temperature show two types of terminations (the fine and coarse structures) on a single terrace. Since the tip condition is unchanged during imaging of the surface, observation of two types of terminations reveal that the surface has not fully equilibrated at lower annealing temperature.